The Aeronautical Journal (2026), 1–20
doi:10.1017/aer.2026.10255

ROYAL AERONAUTICAL SOCIETY

RESEARCH ARTICLE

Research on entry guidance and test methods for reusable launch vehicle

Jingzhi Chen[1,2], Quan Pan[1] and Zibing Du[1,2]

[1]School of Automation, Northwestern Polytechnical University, Xi'an, China
[2]Chinese Flight Test Establishment, Xi'an, China
Corresponding author: Jingzhi Chen; Email: 13720543608@163.com

Received: 18 June 2025 UTC; **Revised:** 6 September 2026 UTC; **Accepted:** 16 September 2026 UTC

Keywords: flight test; guidance law; re-entry; reusable launch vehicle

Abstract

The purpose of the re-entry phase is to reduce excessive speed and altitude to meet the initialisation conditions of the Terminal Area Energy Management (TAEM) phase for a reusable launch vehicle (RLV). The key to re-entry guidance research lies in designing the lateral bank angle profile and the longitudinal angle-of-attack profile. The bank angle profile must be designed to ensure achievement of the total re-entry range, while the angle-of-attack profile should primarily minimise the aerodynamic heating load of the vehicle. In this paper, a guidance law design method based on the drag-energy profile is presented, and the profile is obtained using an optimisation method. A linear control law is derived to track the drag reference; the angle-of-attack and bank angle profiles are developed, and a re-entry flight guidance and control system is established based on a specific vehicle model. Flight simulation results show that the control system works effectively: the RLV can fly to the start of the TAEM phase with a range error of less than 0.2 km, a maximum overload of 1.6 g (meeting the constraint requirement of 2.5 g) and a maximum dynamic pressure of 13 kPa (below the allowable limit of 17 kPa); the trajectory azimuth angle error is limited to within $\pm 18^{\circ}$, which fully verifies the accuracy, safety and feasibility of the proposed guidance method.

Nomenclature

r	radial distance from the centre of the Earth to the RLV
v	Earth-relative velocity
γ	flight-path angle
φ	bank angle
φ_c	reference bank angle
θ	pitch angle
ψ	yaw angle
χ	azimuth angle
α	angle-of-attack
α_c	reference angle-of-attack
β	sideslip angle
D	drag acceleration
D_R	reference drag acceleration
g	gravitational acceleration
u	vertical component of the lift-to-drag ratio
u_R	reference vertical component of the lift-to-drag ratio
s	horizontal range
S	reference area of the wing
e	negative specific energy

© The Author(s), 2026. Published by Cambridge University Press on behalf of Royal Aeronautical Society.

Downloaded from https://www.cambridge.org/core. 18 Nov 2026 at 06:15:15, subject to the Cambridge Core terms of use.

V	airspeed of the vehicle
V_0	initial value of V
ρ	atmospheric density
p	roll rate
q	pitch rate
h	altitude
h_s	reference height coefficient
r	yaw rate
m	mass of the RLV
R_0	radius of the Earth
Δ	deviation
δ_a	increment of the aileron
δ_e	increment of the elevator
δ_r	increment of the rudder
C_D	aerodynamic lift coefficient
C_L	aerodynamic drag coefficient
L/D	lift-to-drag ratio
$(L/D)_c$	reference lift-to-drag ratio
T_δ	coefficients corresponding to $\delta_a, \delta_e, \delta_r$
K_α	coefficients corresponding to α
K_α^i	coefficients corresponding to α_c
K_φ	coefficients corresponding to φ
K_φ^i	coefficients corresponding to φ_c
$K_{\dot\phi}$	coefficients corresponding to $\dot\phi$
K_β	sideslip angle control coefficient
K_γ	flight-path angle control coefficient
K_{p}	bank rate control coefficient
K_{q}	pitch rate control coefficient
X_α	axial force derivative with respect to α
X_θ	axial force derivative with respect to θ
X_h	axial force derivative with respect to h
$X_{\delta e}$	axial force derivative with respect to δ_e
X_V	axial force derivative with respect to V
Z_α	normal aerodynamic derivative with respect to α
$Z_{\delta e}$	normal aerodynamic derivative with respect to δ_e
M_α	pitch moment derivative with respect to α
M_V	pitch moment derivative with respect to V
$M_{\delta e}$	pitch moment derivative with respect to δ_e
M_q	pitch moment derivative with respect to q
Y_β	lateral force derivative with respect to β
Y_φ	lateral force derivative with respect to φ
Y_{p}	lateral force derivative with respect to p
Y_{r}	lateral force derivative with respect to r
L_{r}	rolling moment derivative with respect to r
L_β	rolling moment derivative with respect to β
L_{δ_α}	rolling moment derivative with respect to δ_α
$L_{\delta_{\mathrm{r}}}$	rolling moment derivative with respect to δ_{r}
L_{p}	rolling moment derivative with respect to p
N_{p}	yawing moment derivative with respect to p
N_β	yawing moment derivative with respect to β
N_{δ_α}	yawing moment derivative with respect to δ_α
$N_{\delta_{\mathrm{r}}}$	yawing moment derivative with respect to δ_{r}

Downloaded from https://www.cambridge.org/core. 18 Nov 2026 at 06:15:15, subject to the Cambridge Core terms of use.

Abbreviations

GPM	Gauss pseudospectral method
RLV	reusable launch vehicle
TAEM	terminal area energy management

1.0 Introduction

A reusable launch vehicle (RLV) is capable of hypersonic flight above Mach 5 in near space, offering prominent advantages in low-cost space access and reusable space transportation. The re-entry phase is the most critical and risky flight stage for RLVs, as vehicles endure extremely harsh flight environments involving severe aerodynamic heating, stringent dynamic pressure and deceleration overload constraints. Throughout the entire re-entry process, precise trajectory control is essential to guarantee accurate range coverage and safe terminal area energy management (TAEM) phase access. Nevertheless, complex atmospheric disturbances and time-varying aerodynamic parameters always bring unpredictable deviations to re-entry flight, posing great challenges to the stability, robustness and accuracy of re-entry guidance systems. In view of such practical engineering challenges, it is imperative to develop a high-performance re-entry guidance method that features strong anti-disturbance capability, continuous trajectory transition and adaptive optimisation under multiple constraints.

The core of re-entry guidance research lies in the design of lateral bank angle profiles and longitudinal angle-of-attack profiles [1]. The bank angle profile is tailored to meet the total re-entry range requirement, while the angle-of-attack profile is primarily optimised to mitigate aerodynamic heating of the vehicle. Existing re-entry guidance frameworks can be broadly classified into standard trajectory guidance and predictor-corrector guidance [2, 3].

Standard trajectory guidance relies on precomputed reference trajectories loaded on the onboard computer to achieve precise trajectory tracking during flight. A series of representative studies have realised time-constrained trajectory planning, high-precision analytical solutions and online trajectory regeneration by designing segmented drag acceleration, lift-drag energy and altitude-velocity profiles [4–10]. However, these standard trajectory guidance methods universally adopt segmented parameterisation strategies. Such segmented schemes inevitably lead to discontinuous state transitions between the re-entry phase and the TAEM phase, resulting in poor trajectory continuity. Moreover, the fixed pre-stored reference trajectories lack the ability to adapt to complex aerodynamic disturbances, which significantly degrades the range prediction accuracy and environmental adaptability under variable flight conditions.

Unlike offline trajectory-based methods, predictor-corrector guidance achieves high terminal landing precision through real-time prediction and correction of landing point deviations. It has been widely optimised in terms of computational efficiency, anti-interference performance and control saturation suppression [11–18]. Despite these advancements, existing predictor-corrector guidance still suffers from two non-negligible technical bottlenecks. On the one hand, the iterative prediction procedure imposes a heavy computational burden on the onboard processor, limiting the real-time performance of onboard guidance. On the other hand, most existing drag-based reference profiles are segmented, which fails to generate smooth and natural state transitions matching the TAEM initial conditions, and cannot uniformly and efficiently quantify multiple coupled constraints including surface temperature, overload and dynamic pressure.

Collectively, conventional standard trajectory guidance and predictor-corrector guidance methods exhibit inherent deficiencies in range prediction accuracy, terminal positioning precision and anti-disturbance robustness, which restrict their practical applications in complex and variable re-entry flight environments. To address the aforementioned technical gaps, this paper proposes a novel RLV re-entry guidance method based on drag-energy integrated profiles. Different from traditional segmented drag-velocity profiles, the proposed method establishes a drag acceleration model parameterised by flight energy, and adopts cubic spline curves to fit optimised trajectory feature points, forming a fully continuous, unsegmented re-entry reference profile. Trajectory optimisation is further employed to

Downloaded from https://www.cambridge.org/core. 18 Nov 2026 at 06:15:15, subject to the Cambridge Core terms of use.

solve the optimal drag acceleration sequence while strictly satisfying the global range accuracy requirements [19–21]. On this basis, a linear tracking control law is derived to realise precise tracking of the drag-energy reference profile, with matched angle-of-attack and bank angle guidance profiles are correspondingly designed.

The main innovations and contributions of this study are summarised as follows:

1. A drag-energy integrated reference profile model is constructed, which realises high-precision range prediction under large flight path angle conditions. It effectively overcomes the poor robustness of conventional algorithms against drastic flight condition variations and aerodynamic disturbances, significantly improving the environmental adaptability and prediction accuracy of re-entry guidance.
2. An unsegmented full-domain re-entry trajectory generation strategy is proposed. The terminal state of the re-entry trajectory naturally matches the initial state of the TAEM phase, completely eliminating the state discontinuity and phase mismatch problems existing in traditional segmented trajectory guidance methods.
3. The proposed profile uniformly quantifies multiple critical flight constraints including aerodynamic heating, overload and dynamic pressure with low computational complexity. It avoids the constraint mismatch defects of segmented reference trajectories and achieves an excellent balance among guidance accuracy, real-time performance and multi-constraint compliance.

Numerical simulation results demonstrate that the proposed method can strictly satisfy constraints related to flight range, overload and aerodynamic heating throughout the entire re-entry flight process. It achieves a smooth and stable transition from the re-entry phase to the TAEM phase without artificial segmentation or iterative divergence, and exhibits superior comprehensive guidance performance compared with state-of-the-art re-entry guidance algorithms.

2.0 Guidance concept based on drag-energy profile

In order to derive the re-entry guidance law, we assume that the Earth is spherical and non-rotating. The forces exerted upon the RLV include gravity, aerodynamic lift and drag, while wind disturbances are neglected. The RLV obeys the following dimensionless equations of motion [22–24]:

$$\dot{r} = v \sin \gamma \tag{1}$$

$$\dot{v} = -D - g \sin \gamma \tag{2}$$

$$v\dot{\gamma} = \left(\frac{v^2}{r} - g\right) \cos \gamma + Du \tag{3}$$

where r is the radial distance from the centre of the Earth to the RLV, normalised by the radius of the Earth $R_0 = 6378000m$. The Earth-relative velocity v is normalised by $\sqrt{G_0 R_0}$, where $G_0 = 9.81m/s^2$. The flight-path angle is γ, D and g are the drag acceleration and gravitational acceleration, respectively. The control u is the vertical component of the lift to drag ratio:

$$u = \left(\frac{C_L}{C_D}\right) \cos \varphi \tag{4}$$

where C_D and C_L are the aerodynamic lift and drag coefficients, respectively, and φ is the bank angle.

To achieve the requirement of high re-entry range accuracy, we define the negative specific energy as follows:

$$e = \left(\frac{1}{r}\right) - \left(\frac{v^2}{2}\right) \tag{5}$$

Downloaded from https://www.cambridge.org/core. 18 Nov 2026 at 06:15:15, subject to the Cambridge Core terms of use.

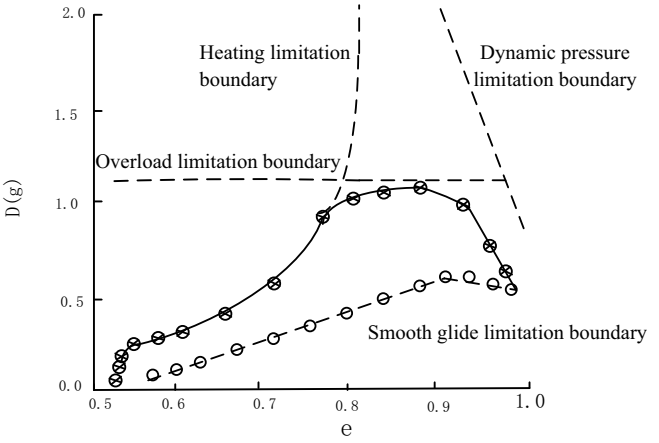


Figure 1. *Drag-energy profile limitation boundary.*

The energy-based drag acceleration delivers higher accuracy in range prediction than the velocity-based drag acceleration profile, the horizontal range satisfies the equation $\dot{s} = v\cos\gamma$, from the definition of $\dot{e} = Dv$, it can be concluded that:

$$ds/de = \cos\gamma/D \tag{6}$$

Also $\cos\gamma \approx 1$, therefore:

$$s \approx \int_{e_0}^{e_f} \frac{1}{D(e)} de \tag{7}$$

From the above equation, one can observe that adopting the drag-energy profile yields an accurate range estimate.

3.0 Determine the bank angle profile

During the re-entry process of an RLV, the bank angle serves as the primary control parameter. The re-entry profile is implemented through the bank angle profile, which underscores the significance of its design. The bank angle profile developed in this paper is based on the drag-energy profile.

First, under the constraints of overload, dynamic pressure and aerodynamic heating, the drag-energy profile is determined using optimisation methods. Next, the obtained drag acceleration profile is converted into a bank angle control command, and the bank angle profile is finally determined by combining the roll direction control logic [22, 23].

The determination of the drag-energy profile is limited by the following factors:

1. Overload limitation. The overload of the RLV needs to meet the design requirements.
2. Heating limitation. To prevent the RLV from thermal failure during re-entry, its surface temperature must not exceed the limit value.
3. Dynamic pressure limitation. To reduce the structural weight of the RLV and the rudder surface loads, the dynamic pressure of the RLV must not be excessively high.
4. Smooth glide limitation. The RLV's re-entry profile shall neither be overly gentle nor violate the smooth–glide boundary.

The boundary restrictions are illustrated in Figure 1; The optimisation method is not discussed in this paper. The re-entry profile is a cubic spline curve fitted by a series of optimal points, which are marked by asterisks in Figure 1.

Downloaded from https://www.cambridge.org/core. 18 Nov 2026 at 06:15:15, subject to the Cambridge Core terms of use.

Once the re-entry profile is determined, the corresponding lift-to-drag ratio at each negative specific energy value can be calculated along the profile, thereby obtaining the lift-to-drag ratio of the RLV in the vertical plane. Using this lift-to-drag ratio as the reference and comparing it against the actual lift-to-drag ratio provided by the RLV navigation system, the required bank angle control command can be derived. The detailed derivation is as follows:

During re-entry, the atmospheric density ρ changes exponentially, with a rate of:

$$\dot{\rho} = -\rho \frac{\dot{r}}{h_s} \tag{8}$$

where h_s represents the reference height coefficient that has been made dimensionless by R_0. The expression for the dimensionless quantity D is as follows:

$$D = \frac{\rho R_0}{(m/S)} \frac{v^2}{2} C_D \tag{9}$$

where m is the mass of the RLV and S is the reference area of the wing.

Assuming C_D is a constant, differentiating Equation (9) and substituting it into Equation (8), the following can be obtained:

$$\frac{\dot{D}}{D} = -\frac{\dot{r}}{h_s} + \frac{2\dot{v}}{v} \tag{10}$$

Differentiating the above equation:

$$\frac{\ddot{D}}{D} = \frac{\dot{D}^2}{D^2} - \frac{\ddot{r}}{h_s} + \frac{2\ddot{v}}{v} - \frac{2\dot{v}^2}{v^2} \tag{11}$$

where $\dot{D}$ represents the first-order derivative of the drag acceleration with respect to time and represents $\ddot{D}$ the second-order derivative of the drag acceleration with respect to time. By differentiating Equation (1), substituting the result into Equations (3) and (10) and adopting the approximate values $\cos\gamma \approx 1$, the vertical acceleration can be expressed as a function of the control variable:

$$\ddot{r} = \frac{\dot{v}}{v}\dot{r} + v\dot{\gamma} = \frac{\dot{v}}{v} h_s \left(\frac{2\dot{v}}{v} - \frac{\dot{D}}{D} \right) + \left(\frac{v^2}{r} - g \right) + Du \tag{12}$$

Substituting Equation (1) into Equation (2):

$$\dot{v} = -D - \frac{g}{v}\dot{r} \tag{13}$$

Substituting Equation (10) into Equation (13), the differential of velocity can be expressed in terms of drag acceleration:

$$\dot{v} = \left(-D + gh_s \frac{\dot{D}}{Dv} \right) \left(1 + \frac{2gh_s}{v^2} \right)^{-1} \tag{14}$$

Ignoring fraction $2gh_s/v^2$, differentiating the above equation:

$$\ddot{v} = -\dot{D} + \frac{gh_s}{v} \left(\frac{\ddot{D}}{D} - \frac{\dot{D}^2}{D^2} - \frac{\dot{D}\dot{v}}{Dv} \right) \tag{15}$$

Substituting Equation (11) into Equation (15):

$$\ddot{v} = -\dot{D} + \frac{gh_s}{v} \left(-\frac{\ddot{r}}{h_s} + \frac{2\ddot{v}}{v} - \frac{2\dot{v}^2}{v^2} - \frac{\dot{D}\dot{v}}{Dv} \right) \tag{16}$$

By substituting Equation (12) into Equation (16) and neglecting higher-order infinitesimal terms, we can obtain:

$$\ddot{v} = -\dot{D} - \frac{g}{v} \left(\frac{v^2}{r} - g \right) - \frac{Dg}{v} u \tag{17}$$

Downloaded from https://www.cambridge.org/core. 18 Nov 2026 at 06:15:15, subject to the Cambridge Core terms of use.

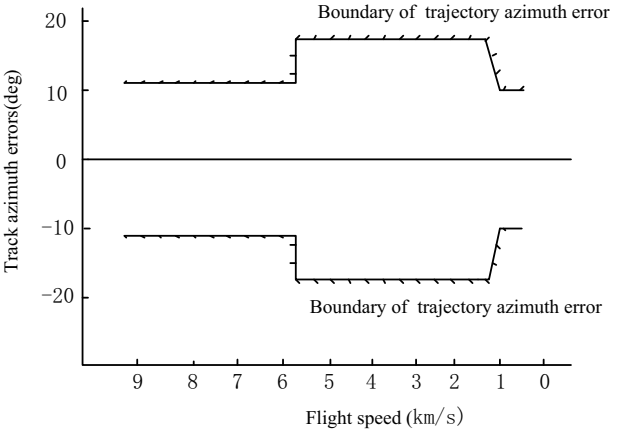


Figure 2. *Allowable range of trajectory azimuth error.*

Substituting Equations (12) and (16) into Equation (11):

$$u = \left[\frac{\dot{D}^2}{D^2} - \frac{\ddot{D}}{D} - \frac{4\dot{v}^2}{v^2} + \frac{\dot{D}\dot{v}}{D\dot{v}} - \frac{2\dot{D}}{v} - \left(\frac{2g}{v^2} + \frac{1}{h_s}\right)\left(\frac{v^2}{r} - g\right)\right]\left(\frac{2Dg}{v^2} + \frac{D}{h_s}\right)^{-1} \tag{18}$$

The reference drag acceleration D_R is given in the drag-energy profile, from Equation (6) and equation $\dot{e} = Dv$, the differential expression of drag acceleration reference can be obtained:

$$\dot{D}_R = D'Dv \tag{19}$$

$$\ddot{D}_R = D''D^2v^2 + \left(D'\right)^2 Dv^2 + D'D\dot{v} \tag{20}$$

where D' represents the first-order partial derivative dD/de of the drag acceleration with respect to e, and D'' represents the second-order partial derivative of the drag acceleration with respect to e and $\dot{v}$ can be calculated from Equation (14), and by substituting D_R, $\dot{D}_R$, and $\ddot{D}_R$ into Equation (18), the reference value u_R of the control variable can be obtained, which is the reference lift to drag ratio $(L/D)_c$.

The actual lift-to-drag ratio is used to track the reference lift-to-drag ratio obtained from Equation (18), and the bank angle of the RLV can be derived from Equation (6):

$$\cos\varphi_c = \frac{(L/D)_c}{L/D} \tag{21}$$

where φ_c is the required bank angle reference profile.

Once the actual and reference lift-to-drag ratios are known, the flight control system can determine the magnitude of the bank angle φ_c. However, the roll direction remains undetermined at this stage, requiring the design of roll direction control logic for its management. RLVs typically ascertain the roll direction based on track azimuth errors. The permissible range for track azimuth errors during re-entry is illustrated in Figure 2. The specific control methodology for roll direction involves the following: within a certain speed range, if the vehicle's track azimuth error exceeds a predefined limit, the vehicle's roll is reversed; otherwise, the current roll direction is maintained. By regulating the roll direction through track azimuth error constraints, the vehicle's lateral distance can be restricted within allowable bounds, ensuring that it consistently heads towards the commencement of the TAEM phase [24, 25]. The bank angle is determined using Equation (21), while the roll direction is defined by track azimuth constraints, ultimately leading to the determination of the bank angle profile. The angle-of-attack profile is illustrated in Figure 2.

Downloaded from https://www.cambridge.org/core. 18 Nov 2026 at 06:15:15, subject to the Cambridge Core terms of use.

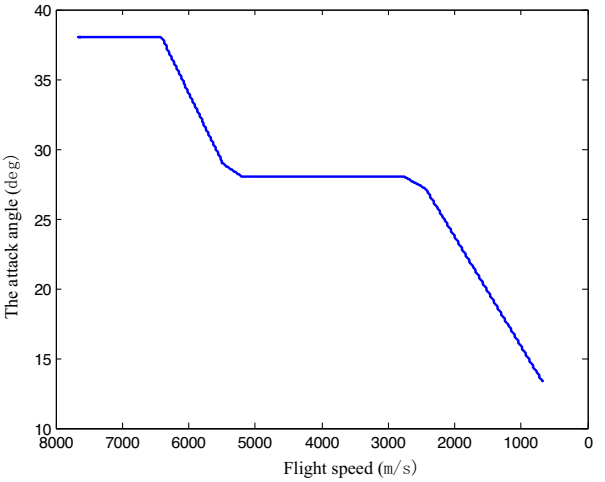


Figure 3. *The attack angle profile of RLV.*

4.0 Determine the attack angle profile

During the re-entry process, the angle-of-attack profile primarily aims to minimise the vehicle's aerodynamic heating. Generally, maintaining a high angle-of-attack during the initial re-entry phase can effectively reduce the load on the vehicle's thermal protection system. Subsequently, the angle-of-attack should gradually decrease as the speed decreases, thereby slowing down the deceleration process, relatively extending the flight duration and improving lateral manoeuvrability [26–28].

The aerodynamic coefficients C_L and C_D for the vehicle are provided in tabulated data as functions of Mach number and angle-of-attack α. For the reference drag profile design, the coefficients are approximated by fitting the data in hypersonic regimes:

$$C_L = -0.062 + 0.023\alpha + 0.0004\alpha^2 \tag{22}$$

$$C_D = 0.092 - 0.025C_L + 0.652{C_L}^2 \tag{23}$$

where α is in degrees. The angle-of-attack is scheduled with respect to velocity. It is first held at a constant of $\alpha = 38$ deg from the initial phase of re-entry ($v = 7600$m/s) to $\alpha = 28$ deg for thermal protection, and then reduced to $\alpha = 13$ deg ($v = 650$m/s) where the handover to the terminal area guidance takes place. The angle-of-attack profile is illustrated in Figure 3.

5.0 The mathematical model of reusable launch vehicle and Lyapunov stability analysis

5.1 The mathematical model of RLV

The mathematical model is divided into longitudinal and lateral motion models, both of which are described by the following state-space equations:

$$\begin{aligned} \dot{x} &= Ax + Bu \\ y &= Cx + Du \end{aligned} \tag{24}$$

where x, u and y represent the state variable, control input and measurement output, respectively.

Longitudinal motion model:

$$\begin{aligned} x_{lon} &= [\Delta v \quad \Delta\alpha \quad \Delta\theta \quad q \quad \Delta h]^T \\ u_{lon} &= \delta_e \\ y_{lon} &= [\Delta v \quad \Delta\alpha \quad \Delta\theta \quad q \quad \Delta h]^T \end{aligned} \tag{25}$$

Downloaded from https://www.cambridge.org/core. 18 Nov 2026 at 06:15:15, subject to the Cambridge Core terms of use.

Where v is the airspeed of the vehicle, α is the angle-of-attack, θ is the pitch angle, q is the pitch rate, h is the altitude, the symbol Δ denotes the deviation and δ_e is the increment of the elevator.

Lateral motion model:

$$\begin{aligned} x_{lat} &= [\Delta\beta \quad \Delta\varphi \quad \Delta\psi \quad p \quad r]^T \\ u_{lat} &= [\delta_a \quad \delta_r]^T \\ y_{lat} &= [\Delta\beta \quad \Delta\varphi \quad \Delta\psi \quad p \quad r]^T \end{aligned} \tag{26}$$

where β is the sideslip angle, φ is the bank angle, ψ is the yaw angle, p is the roll rate, r is the yaw rate, the symbol Δ denotes the deviation, δ_a is the increment of the aileron and δ_r is the increment of the rudder.

In the simulation process of this paper, the longitudinal motion model data used are as follows:

$$A_{lon} = \begin{bmatrix} -0.0062 & -14.7415 & -9.7999 & 0 & 0.0008 \\ 0 & -0.1117 & 0 & 1 & 0 \\ 0 & 0 & 0 & 1 & 0 \\ 0.0046 & -3.3626 & 0 & 0.0374 & 0 \\ -0.0039 & -973.8849 & 973.8921 & 0 & 0 \end{bmatrix}$$

$$B_{lon} = \begin{bmatrix} 0.0038 & -0.0001 & 0 & -0.0680 & 0 \end{bmatrix}^T \tag{27}$$

$$C_{lon} = \begin{bmatrix} 1 & 0 & 0 & 0 & 0 \\ 0 & 57.3000 & 0 & 0 & 0 \\ 0 & 0 & 57.3000 & 0 & 0 \\ 0 & 0 & 0 & 57.3000 & 0 \\ 0 & 0 & 0 & 0 & 1 \end{bmatrix}$$

$$D_{lon} = [0 \quad 0 \quad 0 \quad 0 \quad 0]^T$$

The lateral motion model data is as follows:

$$A_{lat} = \begin{bmatrix} -0.0666 & 0.0100 & 0 & 0.1110 & -0.9938 \\ 0 & 0 & 0 & 1 & 0.1078 \\ 0 & 0 & 0 & 0 & 1.0058 \\ -33.1621 & 0 & 0 & -0.2691 & -0.0747 \\ 1.5804 & 0 & 0 & 0.0141 & -0.1261 \end{bmatrix}, B_{lat} = \begin{bmatrix} 0 & 0 \\ 0 & 0 \\ 0 & 0 \\ -1.0682 & 0.1443 \\ -0.1332 & -0.0398 \end{bmatrix}$$

$$C_{lat} = \begin{bmatrix} 57.3000 & 0 & 0 & 0 & 0 \\ 0 & 57.3000 & 0 & 0 & 0 \\ 0 & 0 & 57.3000 & 0 & 0 \\ 0 & 0 & 0 & 57.3000 & 0 \\ 0 & 0 & 0 & 0 & 57.3000 \end{bmatrix} \tag{28}$$

$$D_{lat} = \begin{bmatrix} 0 & 0 & 0 & 0 & 0 \\ 0 & 0 & 0 & 0 & 0 \end{bmatrix}^T$$

Downloaded from https://www.cambridge.org/core. 18 Nov 2026 at 06:15:15, subject to the Cambridge Core terms of use.

By substituting Equation (25), (27) into Equation (24), we can obtain the differential equations for the longitudinal motion model of the reusable launch vehicle are expressed as follows:

$$\begin{cases} \Delta\dot{v} = -0.0062\Delta v - 14.7415\Delta\alpha - 9.7999\Delta\theta + 0.0008\Delta h + 0.0038\Delta\delta_e \\ \Delta\dot{\alpha} = -0.1117\Delta\alpha + q - 0.001\Delta\delta_e \\ \Delta\dot{\theta} = q \\ \dot{q} = 0.0046\Delta v - 3.3626\Delta\alpha - 0.0374q - 0.068\Delta\delta_e \\ \Delta\dot{h} = -0.0039\Delta v - 973.8849\Delta\alpha + 973.8921\Delta\theta \end{cases} \tag{29}$$

By substituting Equation (26), (28) into Equation (24), we can obtain the differential equations describing the lateral-directional motion model of the reusable launch vehicle are expressed as follows:

$$\begin{cases} \Delta\dot{\beta} = -0.0666\Delta\beta + 0.01\Delta\varphi + 0.111p - 0.9938r \\ \Delta\dot{\varphi} = p + 0.1078r \\ \Delta\dot{\psi} = 1.0058r \\ \dot{p} = -33.1621\Delta\beta - 0.2691p - 0.0747r - 1.0682\Delta\delta_a + 0.1443\Delta\delta_r \\ \dot{r} = 1.5804\Delta\beta + 0.0141p - 0.1261r - 0.1332\Delta\delta_a - 0.0398\Delta\delta_r \end{cases} \tag{30}$$

5.2 The Lyapunov stability analysis for the system

Consider the combined longitudinal-lateral augmented linear system of a re-entry vehicle:

$$\dot{X} = AX + Bu \tag{31}$$

where $X = [x_{lon} \quad x_{lat}]^T, A = \begin{bmatrix} A_{lon} & 0 \\ 0 & A_{lat} \end{bmatrix}, B = \begin{bmatrix} B_{lon} & 0 \\ 0 & B_{lat} \end{bmatrix}, u = \begin{bmatrix} u_{lon} & u_{lat} \end{bmatrix}^T$.

In Equation (31), Bu is an external incentive that does not alter the internal balance of the system. The internal stability is only determined by the state matrix A, and Bu only changes the amplitude of the trajectory motion, without affecting the Lyapunov stability properties of the system itself.

We construct the quadratic Lyapunov function candidate:

$$V(X) = X^T X \tag{32}$$

It is easy to verify that $V(X)>0$ for all $X \neq 0$ and $V(0) = 0$. Thus $V(X)$ is positive definite.

Differentiating $V(X)$ with respect to time yields:

$$\dot{V}(X) = 2X^T\dot{X} = 2X^T\ (AX + Bu) \tag{33}$$

Using the block-diagonal structure, we obtain:

$$\dot{V}(X) = 2{x_{lon}}^T A_{lon} x_{lon} + 2{x_{lat}}^T A_{lat} x_{lat} + 2{x_{lon}}^T B_{lon} u_{lon} + 2{x_{lat}}^T B_{lat} u_{lat} \tag{34}$$

Calculating the specific values under the typical flight condition at Mach 3.3, the longitudinal term is negative semi-definite, and the lateral term is negative definite. Therefore:

$$\dot{V}(X) \leq 0, \quad \forall X \tag{35}$$

which means $\dot{V}(X)$ is negative semi-definite.

Based on Lyapunov's direct method, global Lyapunov stability is proven for the system equilibrium. Eigenvalue analysis confirms that the real parts of all eigenvalues are non-positive, and no unstable dynamic modes emerge during flight. Therefore, the RLV achieves favourable dynamic stability throughout the hypersonic re-entry phase.

In summary, the results from Lyapunov stability analysis and eigenvalue examination collectively reveal that the coupled longitudinal and lateral dynamics of the re-entry vehicle are globally Lyapunov stable, with no divergent modes observed. When subject to external disturbances, all system outputs remain bounded. The studied system fully satisfies the stability specifications for hypersonic re-entry flight, offering solid theoretical fundamentals for the design of subsequent flight control systems.

Downloaded from https://www.cambridge.org/core. 18 Nov 2026 at 06:15:15, subject to the Cambridge Core terms of use.

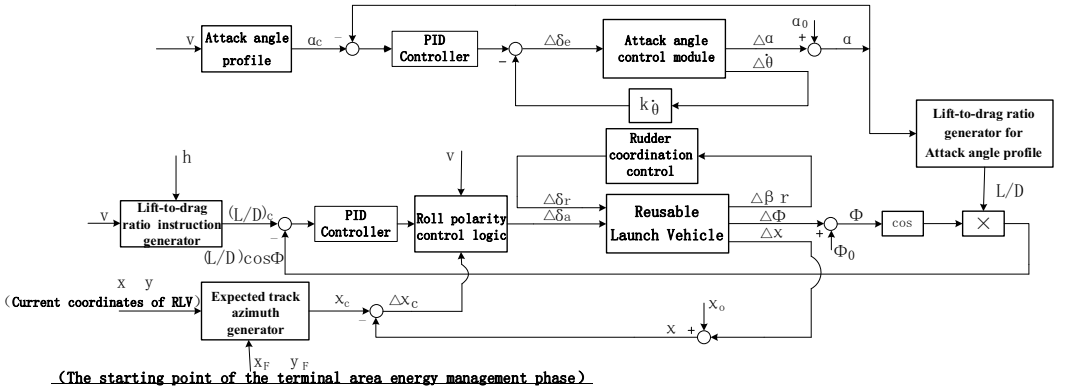


Figure 4. *Guidance and control structure diagram of RLV.*

6.0 The guidance and control system configuration

Guidance commands are processed through flight control laws to derive elevator, aileron and rudder commands. These commands are utilised to manipulate the aerodynamic surfaces of the RLV, thereby controlling its attitude and trajectory [29]. Based on the characteristics of the re-entry phase, an angle-of-attack control system is employed in the longitudinal direction, while a bank angle control system is utilised in the lateral direction. The guidance and control architecture is illustrated in Figure 4. The selection of Proportional, Integral and Derivative (PID) regulators requires comprehensive consideration of performance indicators such as system response speed, steady-state error, overshoot and stability. In practical engineering applications, optimal parameter sets are typically obtained through iterative experimental calibration. The gain selection of a PID controller is determined based on the characteristics of the controlled process to determine the proportional coefficient, integral time and derivative time of the PID controller. Generally, based on engineering experience, gain tuning is directly performed in the control system test, and the method is simple and easy to master. The steps for selecting the gain of a PID controller are as follows: 1) first, select a sufficiently short sampling period for the system to operate; 2) enable only the proportional control loop until the system exhibits critical oscillations in response to a step input; 3) calculate the PID controller gains using standard formulas corresponding to a specific control margin. The detailed control laws are presented below:

1. Vertically, the angle-of-attack control system is employed to track the reference angle-of-attack profile. The control law is as follows:

$$\Delta\delta_e = \frac{1}{T_\delta s + 1}\left[\left(K_\alpha + \frac{K_\alpha^i}{s}\right)(\alpha - \alpha_c) + K_{\dot\theta}\Delta\dot\theta\right] \tag{36}$$

where $\Delta\delta_e$ represents the variation of the elevator, s represents the time, T_δ, K_α, K_α^i and $K_{\dot\theta}$ are the coefficients corresponding to each parameter, α, α_c and $\Delta\dot\theta$ represent the angle-of-attack, reference angle-of-attack and the variation of the pitch rate, respectively.

2. The lateral bank angle control system compares the actual lift-to-drag ratio with the reference lift-to-drag ratio, and the control law is as follows:

$$\Delta\delta_\alpha = \frac{1}{T_\delta s + 1}\left[\left(K_\varphi + K_\varphi^i \frac{1}{s}\right)(\Delta\varphi - \Delta\varphi_c) + K_{\dot\varphi}\Delta\dot\varphi\right] \tag{37}$$

where $\Delta\delta_\alpha$ represents the variation of the aileron, T_δ, K_φ, K_φ^i and $K_{\dot\varphi}$ are the coefficients corresponding to each parameter, $\Delta\varphi$, $\Delta\varphi_c$ and $\Delta\dot\varphi$ represent the variation of bank angle, the reference variation of bank angle and the variation of bank angle derivative.

Downloaded from https://www.cambridge.org/core. 18 Nov 2026 at 06:15:15, subject to the Cambridge Core terms of use.

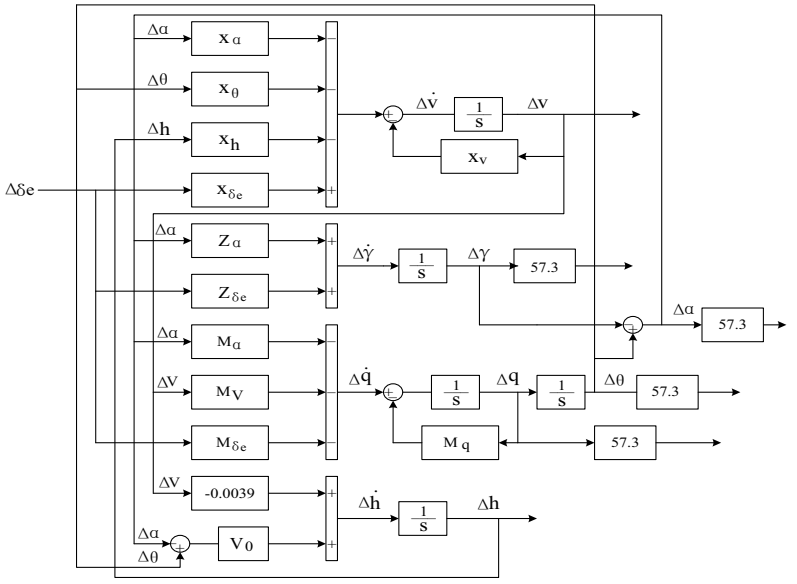


Figure 5. *Longitudinal control structure diagram of RLV.*

3. To eliminate sideslip, rudder coordination control has been incorporated into the lateral system. The control law is as follows:

$$\Delta\delta_r = \frac{1}{T_\delta s + 1}\left[-K_\beta \Delta\beta + \frac{\tau s}{\tau s + 1} K_\gamma \gamma\right] \tag{38}$$

where $\Delta\delta_r$ represents the variation of the rudder, T_δ, K_β and K_γ are the coefficients corresponding to each parameter, $\Delta\beta$ represent the variation of sideslip angle, γ represent the trajectory angle and $\frac{\tau s}{\tau s+1}$ is a cleaning network (high-pass filter).

The polarity control of the bank angle is implemented by the corresponding logic module in Figure 4. This module operates according to the requirements of the trajectory azimuth error limit specified in Figure 2. When the RLV's trajectory azimuth error exceeds the predefined threshold, the module commands the vehicle to reverse its roll direction; otherwise, the current roll orientation is preserved.

In order to ensure the flight stability of the RLV, when the ailerons on the left and right wings deflect in the same direction and angle, symmetrical lift is generated on the left and right wings, thereby forming a pitch moment, which can be used for pitch control or to maintain longitudinal stability. In contrast, differential aileron deflection with varying angles or directions yields asymmetric wing lift, asymmetric lift is generated on the left and right wings, forming a rolling moment that can be used for rolling control or maintaining lateral stability. The two rudder surfaces behind the vertical tail can deflect left and right, generating lateral force and yaw moment, thereby controlling the yaw direction of the nose and maintaining stability.

7.0 Structural configuration of the RLV

7.1 Longitudinal and lateral structural configuration

The longitudinal structural configuration of the RLV model is depicted in Figure 5, while the lateral structural configuration is illustrated in Figure 6. The model's input consists of the RLV's aerodynamic control surfaces, specifically elevators δ_e, ailerons δ_α and rudders δ_r. The output encompasses various RLV states, including altitude h, angle-of-attack α, pitch angle θ, trajectory angle γ, pitch rate q and

Downloaded from https://www.cambridge.org/core. 18 Nov 2026 at 06:15:15, subject to the Cambridge Core terms of use.

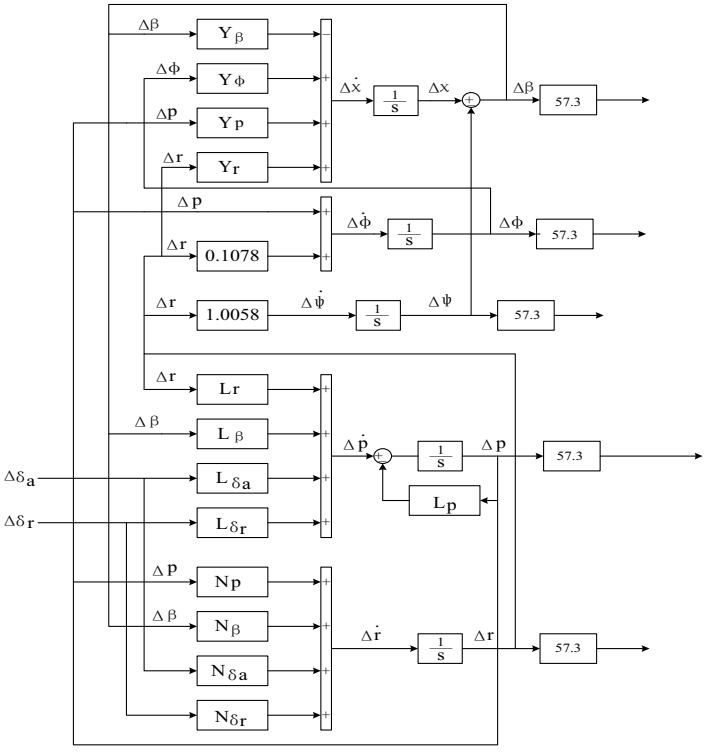


Figure 6. *Lateral control structure diagram of RLV.*

airspeed V. Additionally, the lateral states include sideslip angle β, bank angle φ, track angle χ, yaw angle ψ, bank rate p and yaw rate r, the symbol Δ denotes the deviation.

In Figure 5, parameter $X_\alpha, X_\theta, X_h, X_{\delta e}, X_V$ representing the axial force derivative with respect to the parameters $\alpha, \theta, h, \delta_e, V$, parameter $Z_\alpha, Z_{\delta e}$ representing the normal aerodynamic derivative with respect to the parameters α, δ_e, parameter $M_\alpha, M_V, M_{\delta e}, M_q$ representing the pitch moment derivative with respect to the parameters α, V, δ_e, q, parameter V_0 representing the initial value of V, $\frac{1}{s}$ indicate the integral stage.

In Figure 6, parameter $Y_\beta, Y_\varphi, Y_\mathrm{p}, Y_\mathrm{r}$ representing the lateral force derivative with respect to the parameters β, φ, p, r, parameter $L_\mathrm{r}, L_\beta, L_{\delta_\alpha}, L_{\delta_\mathrm{r}}, L_\mathrm{p}$ representing the rolling moment derivative with respect to the parameters r, $\beta, \delta_\alpha, \delta_\mathrm{r}$, p, parameter $N_\mathrm{p}, N_\beta, N_{\delta_\alpha} N_{\delta_\mathrm{r}}$ representing the yawing moment derivative with respect to the parameters p, $\beta, \delta_\alpha, \delta_\mathrm{r}$.

The above force and moment derivatives represent typical aerodynamic stability derivatives for RLVs. These parameters are acquired jointly via wind tunnel experiments, CFD flow field simulations and engineering identification methods.

7.2 Design of elevator control law

After the guidance instructions are processed through the flight control law, commands for the elevator, aileron and rudder are derived to manipulate the aircraft's aerodynamic control surfaces. The elevator channel is designed to track angle-of-attack commands and translate them into deflection commands for the elevator. The control structure diagram of the elevator is illustrated in Figure 7, K_q is the pitch rate control coefficient.

Downloaded from https://www.cambridge.org/core. 18 Nov 2026 at 06:15:15, subject to the Cambridge Core terms of use.

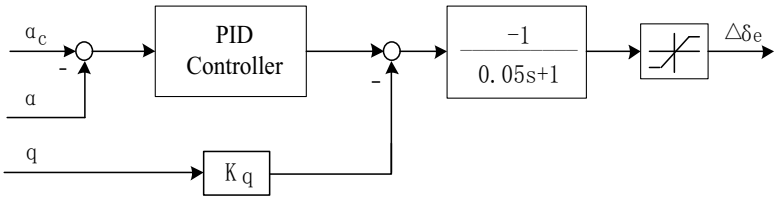


Figure 7. *Elevator control structure.*

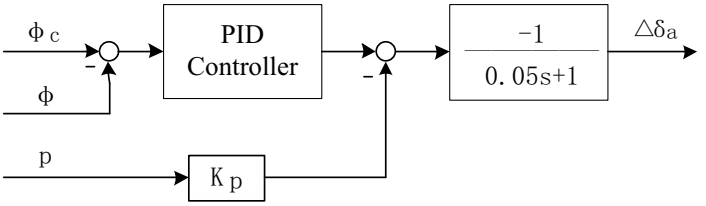


Figure 8. *Aileron control structure.*

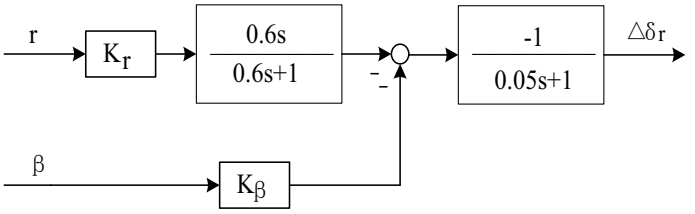


Figure 9. *Rudder coordination control structure.*

7.3 Design of aileron and rudder control laws

The aileron channel is utilised to track bank angle commands, incorporating signals $\dot{\varphi}$ that facilitate 'early counter-steering'. The rudder channel facilitates coordinated turning, enabling the nose to track the velocity vector and eliminate sideslip angles [30, 31]. The feedback r is employed to dampen the rudder channel, thereby minimising the oscillation of the sideslip angle. Additionally, a cleaning network (high-pass filter) $\frac{\tau s}{\tau s+1}$ is incorporated to remove the steady-state component from the rate gyroscope's output signal. The aileron control law and rudder coordinated control structure diagrams are illustrated in Figures 8 and 9, K_p is the bank rate control coefficient and K_β is the sideslip angle control coefficient.

8.0 Simulation experiment verification

The simulation is carried out with the initial conditions of the RLV as follows: an initial height of 119 km, initial azimuth and yaw angles of 45°, an initial angle-of-attack and pitch angle of 38°. Figure 10 displays the longitudinal altitude trajectory of the RLV throughout the entire re-entry flight. The altitude decreases smoothly and monotonically from 119 km to the terminal height without abrupt drops or oscillations, which ensures the stability of the re-entry process and meets the height constraint requirements. Figure 11 illustrates the lateral distance trajectory of the RLV. The lateral displacement changes gently and converges to the target position steadily, demonstrating that the lateral guidance logic can effectively suppress the deviation and achieve accurate lateral trajectory tracking. Figure 12 illustrates the bank angle variation, which is controlled within structural and stability limits. In the initial re-entry phase, it ranges from $-80°$ to $+80°$ with gentle fluctuations for stable attitude transition; in the middle phase, it enters the $-60°$ to $+60°$ range for precise range calibration; in the final phase, it converges smoothly to $-30°$ to $+30°$. The process is continuous, stable, free from severe fluctuations or saturation,

Downloaded from https://www.cambridge.org/core. 18 Nov 2026 at 06:15:15, subject to the Cambridge Core terms of use.

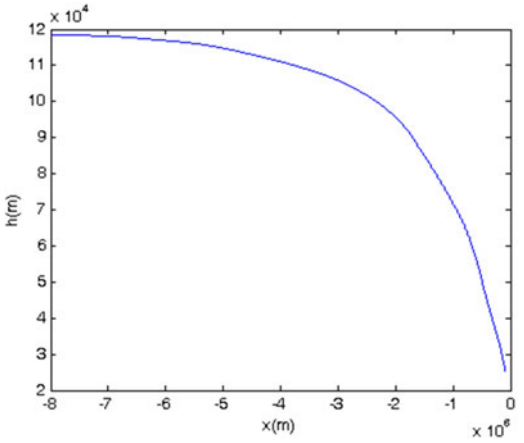


Figure 10. *The altitude trajectory of RLV.*

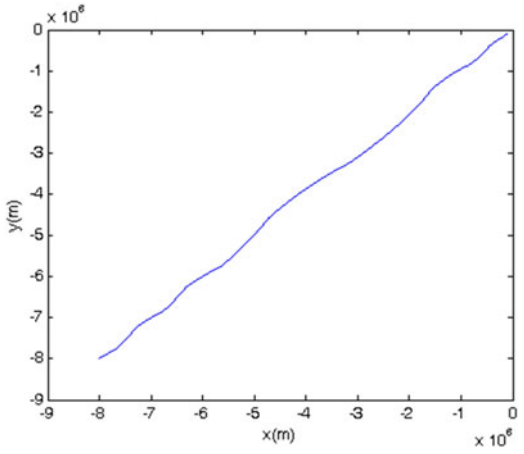


Figure 11. *The lateral trajectory of RLV.*

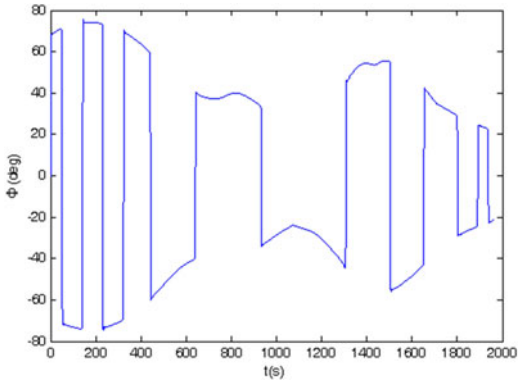


Figure 12. *The bank angle of RLV.*

Downloaded from https://www.cambridge.org/core. 18 Nov 2026 at 06:15:15, subject to the Cambridge Core terms of use.

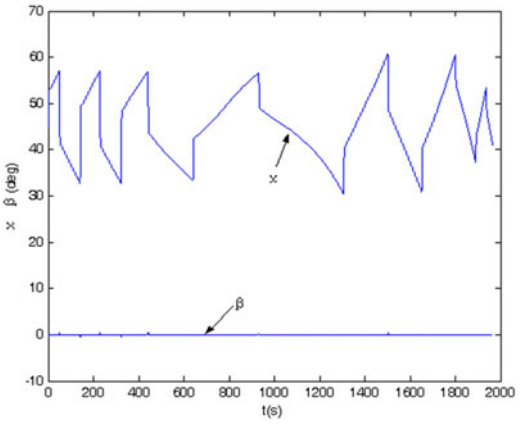


Figure 13. *The azimuth and sideslip angle of RLV.*

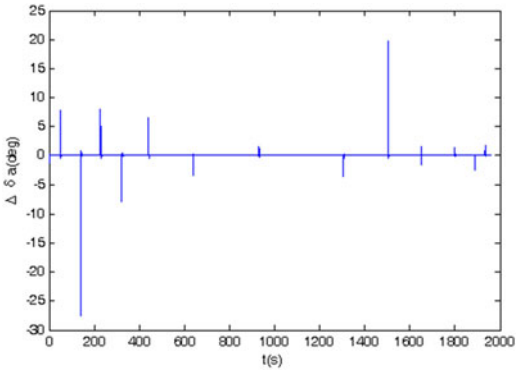


Figure 14. *The process of aileron.*

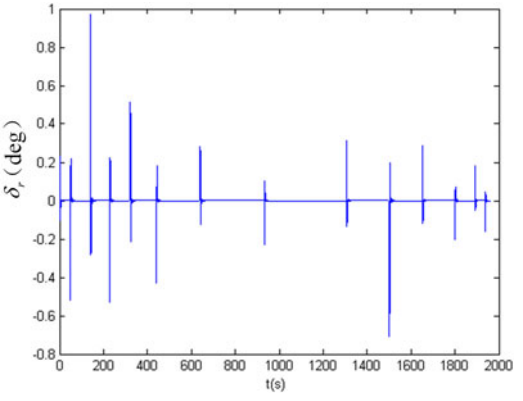


Figure 15. *The process of rudder.*

ensuring stable attitude and reduced aerodynamic coupling interference. Figure 13 shows the trajectory azimuth angle and sideslip angle. The sideslip angle is always maintained near zero during the whole flight, which means strong decoupling performance between longitudinal and lateral channels. The trajectory azimuth angle varies steadily and tracks the reference command accurately. Figures 14 and 15 describe the control processes of the aileron and rudder, respectively. Both control surfaces output smooth and continuous commands without chattering or saturation, which reduces the burden on the

Downloaded from https://www.cambridge.org/core. 18 Nov 2026 at 06:15:15, subject to the Cambridge Core terms of use.

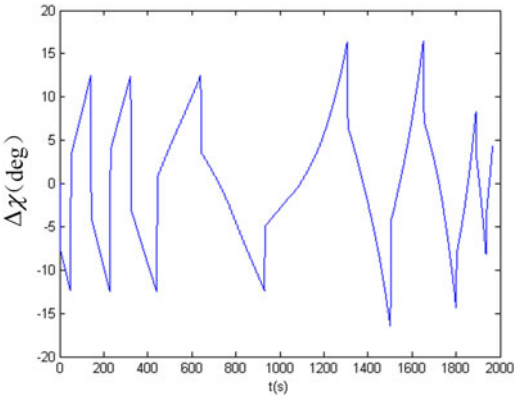


Figure 16. *The trajectory azimuth angle error.*

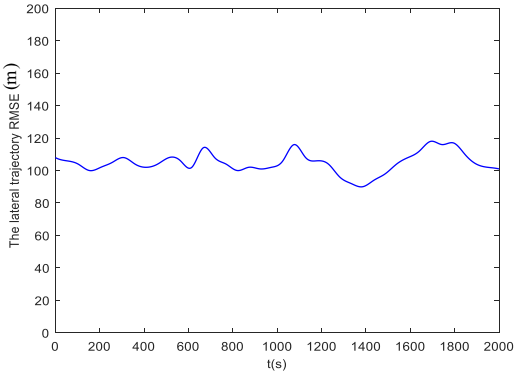


Figure 17. *The lateral trajectory RMSE curve.*

actuator and meets the engineering application requirements. Figure 16 depicts the trajectory azimuth angle error. The error is limited to $\pm 12.5^\circ$ in the high-speed zone, $\pm 18^\circ$ in the medium-speed zone and $\pm 10^\circ$ in the low-speed zone, and converges rapidly to a small range, showing high guidance precision. Figure 17 gives the lateral trajectory root mean square error (RMSE) curve. The RMSE maintains a low level throughout the flight and converges quickly, which proves that the proposed method has high steady-state accuracy and good dynamic tracking performance. At the end of the simulation, the RLV reaches the starting point of the TAEM phase successfully. The range error is less than 0.2 km, the maximum overload is 1.6 g (well within the 2.5 g constraint) and the maximum dynamic pressure is 13 kPa (below the 17 kPa threshold). All constraints are fully satisfied.

Compared with the existing re-entry guidance methods in the literature [4–18], the proposed method exhibits obvious advantages. In terms of trajectory tracking accuracy, the range error and lateral RMSE in this paper are lower than those of standard trajectory guidance and predictor-corrector guidance [5, 7, 12, 15]. In terms of lateral control and sideslip suppression, the sideslip angle is maintained near zero throughout the flight, which is superior to the results with lateral disturbance reported in References [9, 13]. In terms of control smoothness, the aileron and rudder commands are free of saturation and chattering, making the proposed method more suitable for onboard application than methods with frequent fluctuations in control output. In terms of constraint compliance, overload, dynamic pressure and azimuth error all satisfy the engineering indicators, and the stability and robustness are better than those of traditional methods under disturbances.

In terms of dynamic response indicators with respect to simulation time, the rise time of the controller for attitude angle tracking is less than 3 s, and the settling time is within 12 s, which means the

Downloaded from https://www.cambridge.org/core. 18 Nov 2026 at 06:15:15, subject to the Cambridge Core terms of use.

controller can quickly respond to the reference command and enter a stable state in a short time. During the entire simulation period, the overshoot of the attitude angle and trajectory parameters is less than 2%, and there is no obvious oscillation, reflecting good stability and damping performance of the controller. In addition, throughout the simulation process, the controller effectively ensures that the RLV operates within the constraints of overload ($\leq$2.5 g), dynamic pressure ($\leq$17 kPa) and control surface deflection, which further validates the reliability and effectiveness of the controller across the full re-entry simulation duration.

Based on the simulation results, the following conclusions can be drawn:

1. Compared with advanced benchmark methods such as standard trajectory guidance, predictor-corrector guidance and traditional drag tracking methods, the proposed approach achieves superior performance in trajectory-tracking accuracy, lateral control performance and sideslip angle suppression, with smoother control commands and higher computational efficiency.
2. From the perspective of dynamic characteristics, the sideslip angle of the vehicle remains at nearly zero during the simulation, indicating excellent decoupling among the yaw, roll and pitch channels and excellent rudder coordination capability. The lateral disturbances caused by aerodynamic coupling in re-entry are effectively suppressed, and the attitude and trajectory maintain high stability.
3. In terms of constraint satisfaction, control variables such as bank angle, aileron and rudder change smoothly without command saturation or chattering. All re-entry flight constraints, including range, overload and aerodynamic heating, are fully satisfied, which verifies the safety and engineering feasibility of the proposed method.
4. In terms of robustness and disturbance rejection, the system still maintains high-precision trajectory tracking under model uncertainties, parameter perturbations and external disturbances, showing that the proposed guidance strategy has strong robustness and can adapt to complex real flight environments.
5. From the viewpoint of error convergence and steady-state performance, the trajectory azimuth error and lateral trajectory RMSE converge rapidly and stay at a low steady-state level without overshoot or deviation, reflecting the excellent dynamic quality and high precision of the guidance and control system.
6. For engineering application value, the proposed method supports online adjustment of the re-entry reference profile to meet different range and constraint requirements. With low computational burden and strong real-time performance, it is suitable for onboard real-time guidance and presents significant engineering application value.

9.0 Conclusion

This study proposes a re-entry guidance method based on an optimised drag-energy integrated profile and derives a corresponding linear tracking control law, which effectively improves the re-entry trajectory tracking accuracy and environmental adaptability of RLVs. Different from the traditional separate design paradigm of longitudinal and lateral guidance, the proposed method realises the coordinated optimisation of angle-of-attack and bank angle profiles by constructing a fully continuous unsegmented drag-energy reference trajectory, which fundamentally solves the state discontinuity problem of conventional segmented guidance methods. The key innovations of the proposed method are as follows.

First, compared with state-of-the-art standard trajectory guidance and predictor-corrector guidance methods, the proposed method achieves superior re-entry guidance accuracy with quantitative performance advantages. The actual terminal range error is controlled within 0.2 km, and the lateral trajectory

Downloaded from https://www.cambridge.org/core. 18 Nov 2026 at 06:15:15, subject to the Cambridge Core terms of use.

RMSE maintains a low and rapidly convergent level throughout the flight. The trajectory azimuth angle error is limited to $\pm 12.5^\circ$ in the high-speed zone, $\pm 18^\circ$ in the medium-speed zone and $\pm 10^\circ$ in the low-speed zone, which is significantly better than the tracking accuracy of traditional segmented guidance algorithms.

Second, the proposed unsegmented full-domain trajectory generation strategy realises smooth and natural state transition from the re-entry phase to the TAEM phase without artificial segmentation and iterative divergence. The vehicle sideslip angle is stably maintained near zero during the entire re-entry process, realising high-precision decoupling of pitch, roll and yaw channels and effectively suppressing aerodynamic coupling interference and lateral disturbance. The attitude and trajectory fluctuations are completely eliminated compared with conventional guidance methods.

Third, the method strictly satisfies all multi-physical constraint indicators throughout the full flight envelope. The maximum re-entry overload is only 1.6 g, which is far lower than the allowable constraint of 2.5 g; the maximum dynamic pressure is 13 kPa, which is less than the 17 kPa limit. The bank angle varies continuously from $\pm 80^\circ$ (initial phase) to $\pm 30^\circ$ (terminal phase), while the aileron and rudder control outputs are smooth and chattering-free without saturation, achieving a balanced optimisation of guidance accuracy, control stability and constraint compliance.

Fourth, the proposed guidance system possesses excellent dynamic response performance and strong robustness. The attitude angle tracking rise time is less than 3 s and the settling time is within 12 s. The overshoot of all trajectory and attitude parameters is controlled below 2% with no obvious oscillation. Moreover, the method can still maintain high-precision trajectory tracking under model uncertainties and parameter perturbations, which verifies its outstanding anti-disturbance capability and adaptability to complex re-entry environments.

In summary, the proposed method possesses significant engineering application potential. Benefiting from the unsegmented low-complexity drag-energy profile design, the algorithm has low computational burden and excellent real-time performance. It supports the online dynamic adjustment of reference trajectories to accommodate variable range mission demands, fully satisfying the on-board real-time guidance requirements for RLV re-entry flight and demonstrating broad practical application prospects.

Competing interests. The authors declare no conflict of interest of any nature upon the development and publication of this work.

References

[1] Wang, K., Guo, J.L. and Hao, L.Y. Recent status and development review of spacecraft reentry guidance methods, *Flight Dyn.*, 2008, **26**, pp 1–9.

[2] Ding, Y., Yue, X., Chen, G., et al. Review of control and guidance technology on hypersonic vehicle, *Chin. J. Aeronaut.*, 2022, **35**, pp 1–18.

[3] Pan, L., Han, Y., Peng, S., et al. A survey of gliding guidance methods for hypersonic vehicles, *J. Natl. Univ. Def. Technol.*, 2017, **39**, pp 15–22.

[4] Wang, P., Yan, X. and Nan, W.J., et al. A rapid and near analytic planning method for gliding trajectory under time constraints, *Acta Armamentarii*, 2024, **45**, pp 2294–2305.

[5] Zhang, W.Q., Yu, W.B., Li, J.L., et al. Cooperative reentry guidance for intelligent lateral maneuver of hypersonic vehicle based on downrange analytical solution, *Acta Armamentarii*, 2021, **42**, pp 1400–1411.

[6] Mu, L., Yu, X., Zhang, Y.M., et al. Onboard guidance system design for reusable launch vehicles in the terminal area energy management phase, *Acta Astronaut.*, 2018, **143**, pp 62–75.

[7] Zang, L., Lin, D., Chen, S., et al. An on-line guidance algorithm for high L/D hypersonic reentry vehicles, *Aerosp. Sci. Technol.*, 2019, **89**, pp 150–162.

[8] Zhang, Y., Chen, K., Liu, L., et al. Entry trajectory planning based on three-dimensional acceleration profile guidance, *Aerosp. Sci. Technol.*, 2016, **48**, pp 131–139.

[9] Peng, Z.X., Qi, Z.Q. and Li, Y.Y. Powered vehicle entry trajectory optimization based on sequential convex optimization, *Aerosp. Control*, 2024, **42**, pp 43–50.

[10] Wang, K., Guo, J.L. and Hao, L.Y. Research on fixed-trim reentry guidance with multiple constraints, *J. Northwest. Polytech. Univ.*, 2023, **41**, pp 1073–1078.

[11] Xu, H., Cai, G., Mu, C., et al. Segmented predictor-corrector reentry guidance based on an analytical profile, *J. Zhejiang Univ.-Sci. A*, 2025, **26**, pp 50–65.

Downloaded from https://www.cambridge.org/core. 18 Nov 2026 at 06:15:15, subject to the Cambridge Core terms of use.

[12] Liu, Z., Zheng, G., Zhang, B., et al. Predictor-corrector reentry guidance for hypersonic glide vehicles based on high-precision analytical solutions, *Aerosp. Sci. Technol.*, 2024, **155**, p 109545.
[13] Zhang, K., Shi, G.X. and Wang, P. Predictor-corrector reentry guidance with cross-range dynamic constraint, *J. Astronaut.*, 2020, **41**, pp 429–437.
[14] Zhou, H., Li, X., Bai, Y., et al. Optimal guidance for hypersonic vehicle using analytical solutions and an intelligent reversal strategy, *Aerosp. Sci. Technol.*, 2023, **132**, p 108053.
[15] Liang, Z. and Zhu, S. Constrained predictor-corrector guidance via bank saturation avoidance for low L/D entry vehicles, *Aerosp. Sci. Technol.*, 2021, **109**, p 106448.
[16] Zhang, J.L., Liu, K., Fan, Y.Z., et al. A piecewise predictor-corrector re-entry guidance algorithm with no-fly zone avoidance, *J. Astronaut.*, 2021, **42**, pp 122–131.
[17] Zhang, J., She, Z., Fan, Y., et al. Numerical predictor-corrector re-entry guidance algorithm for aerospace vehicles, *IEEE International Conference on Unmanned Systems (ICUS)*, 2019, pp 750–755.
[18] Huang, H., Yang, Y., Wu, H., et al. A predictor–corrector entry guidance method using gaussian integration, *2021 40th Chinese Control Conference (CCC)*, 2021, pp 3553–3557.
[19] Jansch, C. and Markl, A. Trajectory optimization and guidance for a Hermes-type reentry vehicle, *Proceedings of the 1991 AIAA Guidance, Navigation and Control Conference, AIAA Washing-DC*, 1991.
[20] Lu, P. Entry guidance and trajectory control for reusable launch vehicle, *J. Guid. Control Dyn.*, 2012, **20**, pp 143–149.
[21] Roenneke, A.J. and Markl, A. Re-entry control of a drag vs energy profile, *J. Guid. Control Dyn.*, 1994, **17**, pp 916–928.
[22] Chen, K.J., Liu, L.H. and Meng, Y.H. *Launch Vehicle Flight Dynamics and Guidance*, National Defense Industry Press, 2014, Changsha, pp 326–334.
[23] Lu, P. Entry guidance: a unified method, *J. Guid. Control Dyn.*, 2014, **37**, pp 713–728.
[24] Wang, X., Guo, J. and Tang, S.J. Analytical reentry guidance method based on quasi-equilibrium glide, *Acta Armamentarii*, 2019, **40**, pp 58–67.
[25] Wang, Z.B. Optimal trajectories and normal load analysis of hypersonic glide vehicles via convex optimization, *Aerosp. Sci. Technol.*, 2019, **87**, pp 357–368.
[26] Yu, W.B., Yang, J. and Chen, W.C. Entry guidance based on analytical trajectory solutions, *IEEE Trans. Aerosp. Electron. Syst.*, 2022, **58**, pp 2438–2466.
[27] Chen, Y.D., Wang, J.N., Shan, J.Y., et al. Cooperative guidance for multiple powered missiles with constrained impact, *J. Guid. Control Dyn.*, 2021, **44**, pp 825–841.
[28] Tahk, M.J., Shim, S.W., Hong, S.M., et al. Impact time control based on time-to-go prediction for sea-skimming antiship missiles, *IEEE Trans. Aerosp. Electron. Syst.*, 2018, **54**, pp 2043–2052.
[29] Guo, Y.H., L.I., X., Zhang, H.J., et al. Entry guidance with terminal time control based on quasi-equilibrium glide condition, *IEEE Trans. Aerosp. Electron. Syst.*, 2019, **56**, pp 887–896.
[30] Geng, K.D., Zhou, J. and Lin, P. Design of rolling-guidance law using virtual target with control of terminal azimuth for a fixed-trim vehicle, *J. Solid Rocket Technol.*, 2015, **38**, pp 320–325.
[31] Li, Z.X., Li, G.F. and Huang, R.L. A vehicle rolling-guidance law based on fixed trimmed angle of attack, *Aerosp. Control Appl.*, 2012, **38**, pp 23–26.

Cite this article: Chen J., Pan Q. and Du Z. Research on entry guidance and test methods for reusable launch vehicle. *The Aeronautical Journal*, https://doi.org/10.1017/aer.2026.10255

Downloaded from https://www.cambridge.org/core. 18 Nov 2026 at 06:15:15, subject to the Cambridge Core terms of use.